1

Title: Low Coseismic Friction on the Tohoku-oki Fault Determined from Temperature Measurements

Authors: Fulton, P. M.[1*], E. E. Brodsky[1], Y. Kano[2], J. Mori[2], F. Chester[3], T. Ishikawa[4], R. N. Harris[5], W. Lin[4], N. Eguchi[6], S. Toczko[6] and the Exp. 343/343T and KR13-08 Scientists

Affiliations:

[1]Dept. of Earth & Planetary Sciences, University of California, Santa Cruz.

[2]Disaster Prevention Research Institute, Kyoto University, Japan.

[3]Center for Tectonophysics, Department of Geology and Geophysics, Texas A&M University, College Station, USA.

[4] Kochi Institute for Core Sample Research, Japan Agency for Marine-Earth Science and Technology, Kochi, Japan.

[5] Oregon State University, Corvallis, Oregon, USA.

[6] Center for Deep Earth Exploration, Japan Agency for Marine-Earth Science and Technology, Yokohama, Japan.

*Correspondence to: pfulton@ucsc.edu

Abstract: The frictional resistance on a fault during slip controls earthquake dynamics. Friction dissipates heat during an earthquake; therefore the fault temperature after an earthquake provides insight into the level of friction. The JFAST project (IODP Expedition 343/343T) installed a borehole temperature observatory 16 months after the March 2011 M_w9.0 Tohoku-oki

23   earthquake across the fault where slip was ~50 m near the trench. After 9 months of operation,

24   the complete sensor string was recovered. A 0.31°C temperature anomaly at the plate boundary

25   fault corresponds to 27 MJ/m^2 of dissipated energy during the earthquake. The resulting apparent

26   friction coefficient of 0.08 is considerably smaller than static values for most rocks.

27

28   **One Sentence Summary:** A 0.31°C temperature anomaly on the Tohoku-oki Earthquake plate

29   boundary fault shows coseismic friction was extremely low.

30

Main Text:

30

31   Earthquake rupture propagation and slip are moderated by the dynamic shear resistance on the

32   fault. Any complete model of earthquake growth therefore requires quantification of shear stress,

33   which is difficult to measure. Historically, the shear stress during an earthquake was thought to

34   be nearly equal to that controlled by static friction, but recent laboratory experiments and field

35   observations have brought this assumption into question (*1,2*). Direct measurement of the

36   magnitude of earthquake stress is challenging because seismological measurements only record

37   stress changes.

38   Rapid response drilling provides a solution (*3*). Because the frictional stress during slip results

39   in dissipated heat, subsurface temperature measurements soon after a major earthquake can

40   record the temperature increase over the fault and its decay. If the slip on the fault is known, the

41   thermal observations allow us to infer the frictional shear stress (*4*, *5*). On 15 July 2012, as part

42   of the JFAST project (Integrated Ocean Drilling Program Expedition 343/343T), we installed a

43   subseafloor temperature observatory in the Japan Trench through the plate boundary fault zone

44   (Hole C0019D) (Fig. 1), which was identified through logging and coring in two adjacent

45   boreholes ~30 m away along strike (Holes C0019B and C0019E, respectively) (SM text; *6*). The

46   deep-sea drilling vessel *Chikyu* developed procedures to allow drilling and installation of the

47   observatory at the requisite 6900 m water depth, making it the deepest open-ocean borehole

48   observatory. The observatory consisted of a string of 55 temperature-sensing dataloggers with

49   <0.001°C accuracy that extended beneath the seafloor in a fully cased 3.5" inner diameter

50   borehole (Fig. 1). Ten of the instruments also recorded pressure at <1000 Pa accuracy to provide

51   control on sensor depths.

52   On 26 April 2013, the JAMSTEC vessel *R/V Kairei* recovered the observatory sensor string

53   with the remotely operated vehicle *Kaiko7000II*. All 55 sensors and the sinker bar were

54   recovered from a maximum depth of 820.6 mbsf. The water depth of the observatory is ~8 m

55   deeper than the adjacent coring and logging holes and thus the fault depth relative to the seafloor

56   is expected to be shallower than observed in logging and coring. The successful recovery implies

57   that there was negligible afterslip or distributed deformation in the borehole 16-25 months after

58   the mainshock.

59   The temperature data reveal a background geothermal gradient of $26.29 \pm 0.13^{o}C$ /km within

60   the region of $650 - 750$ mbsf resulting in a vertical heat flow value of 30.50 ± 2.52 mW/m^2 when

61   combined with thermal conductivity of 1.16 ± 0.09 W/m/^{o}C over this interval (SM Methods).

62   The temperature from 812 m to the bottom at 820 m is elevated by as much as $0.31^{o}C$ relative to

63   this background gradient (Fig. 2). This is the largest temperature anomaly within the dataset and

64   centered on 819 mbsf at the stratigraphic level estimated for the décollement fault zone (6,7).

65   We interpret the temperature anomaly as the frictional heat from the 2011 Tohoku Earthquake.

66   This signal is larger than previous rapid response measurements of frictional heat across a fault

67   after an earthquake (*4, 5*) and is temporally resolved so that its transient nature is distinguished.

68   The temperature data record the combination of the background geotherm, the decaying

69   signature of frictional heating during the 2011 Tohoku Earthquake, and transient effects caused

70   by drilling the borehole and hydrologic processes. Low temperatures relative to the background

71   geotherm early in the experiment (Fig. 2) reflect the effects of water circulation during drilling

72   and equilibration of the observatory upon installation. Because this drilling disturbance acts as a

73   line source compared to the plane or slab source from frictional heating on the fault, its

74   characteristic diffusion time is significantly shorter, allowing measurement of the frictional heat

75   during the 9-month observatory experiment (*8,9,* SM text).

76   To connect the temperature data to the stress on the fault during slip, we modeled the

77   combined effects of the drilling disturbance and frictional heating on the evolution of the

78   temperature field over time and find the energy during the earthquake dissipated as heat that

79   maximizes the normalized cross-correlation between simulations and data (SM text; Fig. 3).

80   Parameter values are constrained by independent drilling and material properties data (SM text;

81   Table S1).

82   From an inversion exploring a wide range of depths, the preferred location of the frictional

83   boundary is 821.3 mbsf which is 7718.8 meters below mean sea level (7717.8-7719.6 mbsl 90%

84   confidence interval, SM text, Table S2). The inversion places the fault below the deepest data

85   logger because the width of the predicted temperature anomaly requires extension to depth for

86   the homogenous thermal properties used here. However, the peak of the temperature anomaly

87   appears to be above the deepest temperature sensor in the data of Fig. 2, and the width of the

88   anomaly may be governed by thermal property structure not included in our model. If we

89   constrain the inversion to require the fault to lie near the peak in temperature above the deepest

90   sensor, the preferred location is 819.8 mbsf (7717.3 mbsl). In either case, the inferred depth of

91   the fault in the observatory hole from the frictional heat is above the hard chert as inferred from

92   the rate of penetration during drilling. The fault inferred from the temperature data is at the same

93   stratigraphic level as the plate boundary fault found in the neighboring coring and logging holes

94   (6,7).

95   The depth-constrained inversion results in an overlapping range of 27 MJ/m^2 (19-51 MJ/m^2

96   90% CI) of dissipated frictional heat energy during the earthquake along the plate boundary (Fig.

97   3). The unconstrained inversion of the temperature observations indicates 31 MJ/m^2 (20-69

98   MJ/m^2 90% CI) (Figs. S4 – S6). In both cases, the dissipated energy in this region of highest slip

99   along the trench (*10*) is comparable to the spatially-averaged radiated energy from the

100   earthquake of 6-17 MJ/m^2 (*11*, *12*) (SM text).

101   Alternative interpretations for a positive temperature anomaly around a fault include the

102   effects of locally reduced thermal conductivity or advection of heat by fluid flow up a permeable

103   fault zone. The magnitude and scale of the observed anomaly, however, is unlikely the result of

104   thermal conductivity differences; the high thermal gradient within the ~20 m zone would require

105   a thermal conductivity of 0.73 W/m/^{o}C, in contrast to values of 1.14 ± 0.07 W/m/^{o}C measured on

106   core samples from comparable intervals in hole C0019E. Rather than a large decrease at the fault

107   zone, measurements throughout the hanging wall and footwall intervals covered by the sensors

108   reveal relatively uniform values before a sharp increase to 1.40 ± 0.19 W/m/^{o}C within chert

109   beneath the sensor string at >829 mbsf (Figure S2). Assuming similar composition, a value of

110   0.73 W/m/^{o}C would require a bulk porosity of ~80-86%. Even if the fault zone is dominated by

111   fractures, such large porosities over tens of meters are unlikely and not supported by logging data

112   or cores recovered from adjacent boreholes.

113   Fluid flow up a fault conduit may also result in a positive temperature anomaly, as is observed

114   at 784 mbsf (Fig. 2). Generalized models of the effects of fluid flow on a frictional heat signal

115   after an earthquake have shown that large flow velocities resulting from a combination of high

116   permeabilities (>10^{-14} m^2) and driving overpressures are required (*9*). High permeability around

117   784 mbsf is indicated by resistivity logs and prolonged drilling anomaly decay time (*13;* Fig.

118   S9). Zones of high permeability, most susceptible to the transient drilling disturbance, are also

119   inferred around 765, 800 and 810 mbsf.

120   None of these indications of high permeability are present at the depth of the inferred slip zone

121   ~820 mbsf, and additional pore fluid chemistry data confirm little fluid flow along the plate

122   boundary (SM text, Fig. S9). The sudden cooling of the anomaly at 784 mbsf after a large local

123   earthquake on 7 December 2012, and the corresponding heating of a high permeability zone at

124   763 mbsf, are consistent with the upward propagation of a fluid pulse driven by either direct

125   stresses or permeability-altering effects of the December 2012 earthquake that changed the

126   preferred flow path for fluids (*14,15*). This interpretation is consistent with borehole images in

127   the interval that show steeply dipping structures conducive to vertical migration of fluids (*13*).

128   Spatially-correlated temperature variations within these permeable zones during times of

129   suspected advective fluid flow are suggestive of episodic fluctuations in flow velocity. Such

130   large variations are not observed within the décollement. At 784 mbsf, the standard deviation of

131   roughly daily to weekly variability is 100% greater than within the décollement before the

132   December earthquake, and at 763 mbsf it is 60% greater after the earthquake [SM text].

133   The time after the earthquake in which the temperature observations were made is many times

134   as large as the characteristic diffusion time across the slip zone for reasonable estimates of slip

135   zone thickness. Therefore, the measurable temperature anomaly from frictional heating is

136   independent of the slip zone thickness and slip duration and does not directly constrain these

137   parameters [SM text]. However, by assuming slip duration ≥ 50 s and slip zone thickness ≥ 1

138   mm, we estimate the maximum peak temperature within the slip zone at this location to be

139   <1250 $^{\circ}$C [SM Methods] (Fig. S7).

140   The geotherm itself also provides a constraint on the long-term integrated energy dissipated on

141   the fault zone (*16,17*). The conductive vertical heat flux of 30.50 ± 2.52 mW/m^2 measured here

142 is consistent with subduction thermal models with very little to no long-term displacement-

143 averaged dissipated energy in the form of heat along the plate boundary (*17*).

144   The dissipated energy is the earthquake parameter best constrained by the temperature data;

145 however, laboratory experiments and theoretical models are often based on the coefficient of

146 friction. For a total of 50 m of slip on the fault (*10*), our best estimate of 27 MJ/m^2 of local

147 dissipated energy during the earthquake implies an average shear stress of 0.54 MPa. In order to

148 compare our results to other studies, we assume an effective normal stress of 7 MPa based on the

149 fault's depth, hydrostatic pore pressure, and measured rock densities, to infer the equivalent

150 coseismic coefficient of friction [SM text]. The resultant apparent coefficient of friction is 0.08.

151 The result is "apparent" because the effective normal stress is inferred from estimates of pore

152 pressure and fault dip [SM text]. The very low values of shear stress and apparent coefficient of

153 friction, which represent displacement averages during the earthquake, are consistent with values

154 determined from high-velocity (1.3 m/s) friction experiments on the Japan Trench plate

155 boundary fault material (*18*).

156   An average shear stress during slip of 0.54 MPa and apparent coefficient of friction of 0.08, as

157 constrained by a measured frictional heat anomaly ~1.5 years after the Tohoku-oki earthquake,

158 suggests that either friction on the fault is remarkably low throughout the seismic cycle or that

159 there was near total stress release at the JFAST location (*19, 20)*. This very low shear resistance

160 during slip may help explain the large slip at shallow depths that contributed to the large

161 devastating tsunami.

162

163 **Figure 1: Observatory configuration.** The observatory sensor string of 55 temperature-sensing

164 dataloggers attached to a rope was installed within 3.5" steel casing that is open at the seafloor

165 and has a check-valve at the bottom preventing inflow of fluid.

166

167

168 **Figure 2: Subseafloor residual temperature field**. (A) Time/space map of data >650 mbsf.

169 Yellow dots show sensor positions and each row represents the corresponding sensor's data.

170 Each column is the daily average temperature after an average background geotherm is removed

171 (SM text). A local M_w7.4 earthquake occurred 17:18:30 JST on 7 Dec 2012 (dashed line). The

172 second deepest sensor (818.51 mbsf) failed on 22 Sept 2012; subsequent data in that row is

173 interpolated from sensors 1.5 m above and below. Periods of no data collection are otherwise

174 shown by white. Sensors at 700 and 781 mbsf were programmed to only record for ~2.5 week

175 periods at 1 Hz sampling rate. Data including five broadly-spaced shallower depths are included

176 in Figure S1. (B) Depth profiles of residual temperature (i.e. with background geotherm

177 removed) from five dates through the experiment separated by two month intervals. The times

178 correspond to the vertical tick marks in Fig. 2A. The y-axis is expanded compared to Fig. 2A

179 showing data from >740 mbsf. Relatively cool temperatures in August reflect the effects of

180 drilling disturbance.

181

182

183 **Figure 3. Time/space map of residual temperature near inferred slip zones.** (A) Following

184 Figure 2A, a close-up view of the residual temperature anomaly near the plate boundary from 1

185   August - 6 December 2012. (B) Simulated residual temperature from model inversions in which

186   fault depth is constrained. Similar results from an inversion in which fault depth is unconstrained

187   are shown in Fig. S4.

188

189   **References and Notes:**

190   1. J. Byerlee, *Pure and Applied Geophysics* **116**, 615–626 (1978).

191   2. G. di Toro et al., *Nature* **471**, 494-498 (2011).

192   3. E. E. Brodsky, K.-F. Ma, J. Mori, D. M. Saffer, *Scientific Drilling* (2009),
193   doi:10.2204/iodp.sd.8.11.2009.

194   4. Y. Kano *et al.*, *Geophys Res Lett* **33**, L14306– (2006).

195   5. H. Tanaka *et al.*, *Geophys Res Lett* **33**, 16316 (2006).

196   6. Chester et al., companion paper.

197   7. The depth interval from which a 1.15 m core of scaly-clay, identified as the fault zone in the
198   companion paper (Chester et al.), extends from 7709.5 mbsl to 7714.3 mbsl in the coring hole 30
199   m away. In the logging hole the fault is interpreted at 7709.5 – 7711.5 mbsl, 15-17 m above a
200   decrease in rate of penetration associated with entering a hard chert layer at 7726.5. A similar
201   decrease in rate of penetration in the observatory hole is observed at 7727.5 mbsl. All depth
202   correlations between holes contain an estimated several meters of uncertainty due to fluctuations
203   of the ship's absolute elevation, flexure of the 7 km of drill stand, borehole deviation, layer
204   thickness variations and fault dip.

205   8. E. Bullard, *Geophys J Int*, 127–130 (1947).

206   9. P. M. Fulton, R. N. Harris, D. M. Saffer, E. E. Brodsky, *J Geophys Res* **115**, B09402 (2010).

207   10. T. Fujiwara *et al.*, *Science* **334**, 1240–1240 (2011).

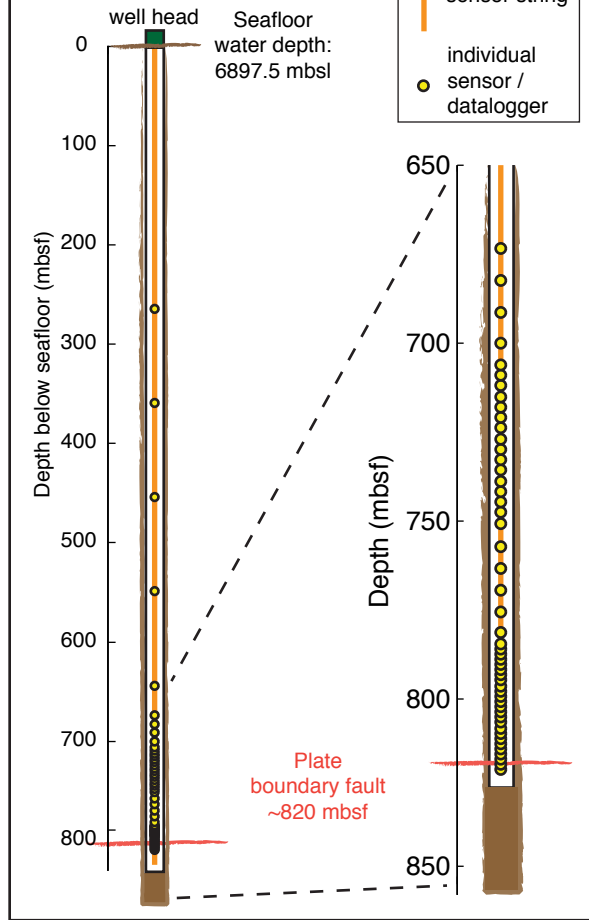208   11. T. Lay, H. Kanamori, *Physics Today* **64**, 33–39 (2011).

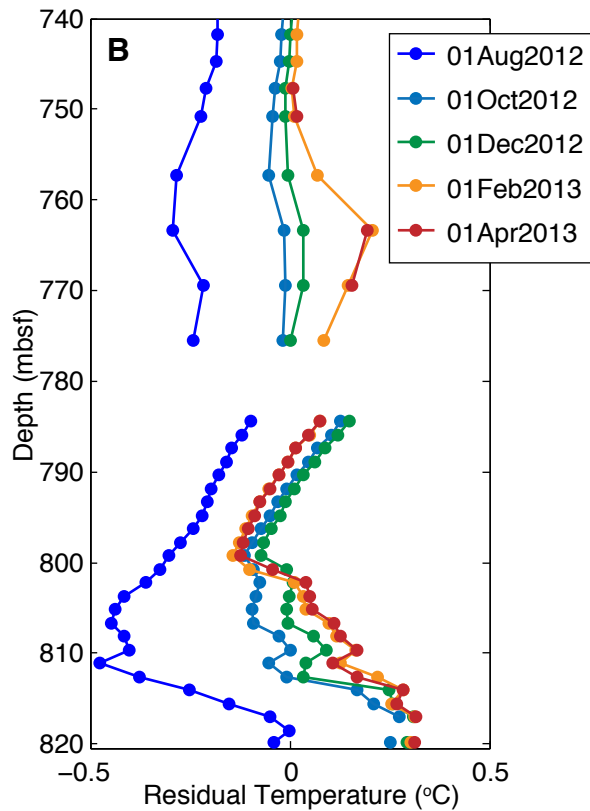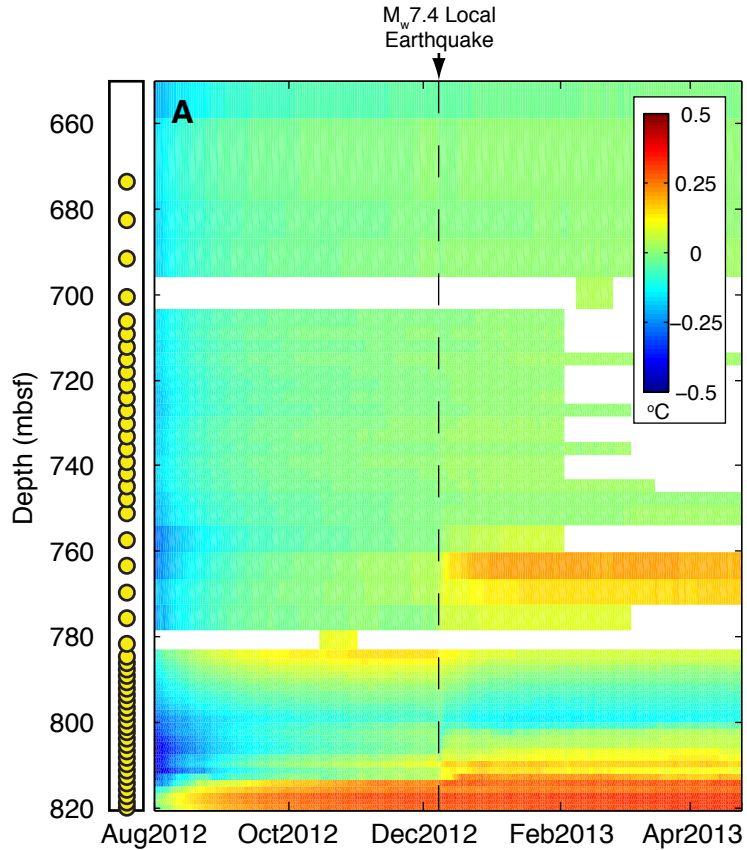209   12. S. Ide, A. Baltay, G. C. Beroza, *Science* **332**, 1426–1429 (2011).

210   13. F. M. Chester, J. J. Mori, S. Toczko, N. Eguchi, the Expedition 343/343T Scientists, Japan
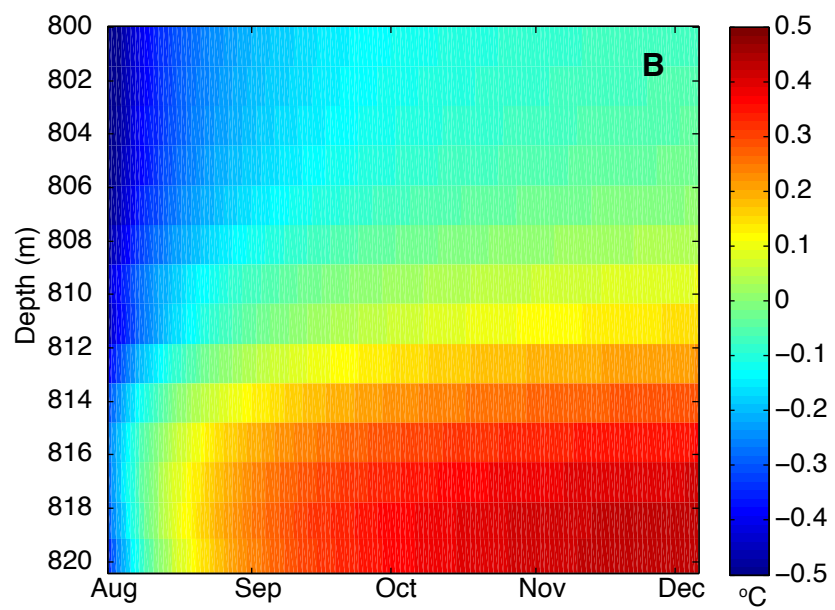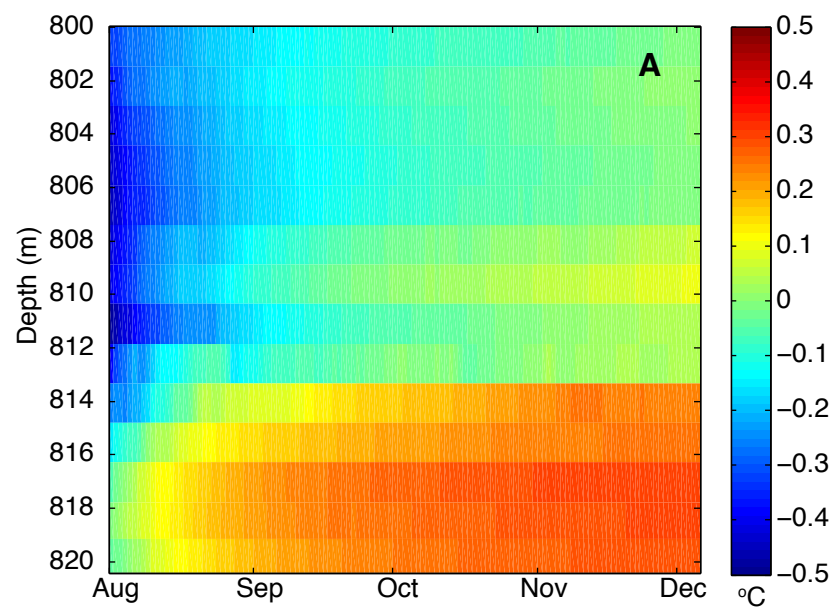211   Trench Fast Drilling Project (JFAST). *IODP Proceedings* 343/343T (2013).

212   14. C.Y. Wang and M. Manga (2010) *Earthquakes and Water*, Lecture Notes Earth Sci. Ser., vol.
213   114, 249 pp., Springer, Berlin.

214   15. J. Elkhoury, E. Brodsky, D. Agnew, *Nature* 441, 1135–1138 (2006).

215   16. K. Wang, T. Mulder, G. C. Rogers, R. D. Hyndman, *J Geophys Res* 100, 12907–12918
216   (1995).

217   17. G. Kimura et al., *Earth and Planetary Science Letters* 339-340, 32–45 (2012).

218   18. Ujiie et al., companion paper.

219   19. K. Wang, K. Suyehiro, *Geophys Res Lett* 26, 2307–2310 (1999).

220   20. W. Lin et al., *Science* 339, 687–690 (2013).

221   21. G. R. Beardsmore, J. P. Cull, *Crustal Heat Flow* (Cambridge University Press, 2001).

222   22. H. S. Carslaw, J. C. Jaeger, *Conduction of heat in solids* (Oxford: Clarendon Press, 1959, 2nd
223   ed., 1959).

224   23. R. H. Sibson, *B Seismol Soc Am* **93**, 1169–1178 (2003).

225   24. H. Kanamori, E. Brodsky, The physics of earthquakes, *Reports on Progress in Physics* **67**,
226   1429 (2004).

227   25. P. M. Fulton and R. N. Harris, *Earth and Planetary Science Letters* 335-336, 206-215
228   (2012).

229   26. A. Lachenbruch, Geological Survey US, Simple models for the estimation and measurement
230   of frictional heating by an earthquake (1986).

231   27. M. Kastner, H. Elderfield, W.J. Jenkins, J.M. Gieskes, T. Gamo, *Proceeding of the Ocean*

232   *Drilling Program, Scientific Results* 131, 397-413 (1993).

233   28. M. Ikari et al., paper presented at the Japan Geoscience Union Meeting 2013, Makuhari,
234   Chiba, Japan, 19 May 2013.

JFAST Observatory

well head

Seafloor water depth: 6897.5 mbsl

sensor string

individual sensor / datalogger

Depth below seafloor (mbsf)

0
100
200
300
400
500
600
700
800

Plate boundary fault ~820 mbsf

Depth (mbsf)

650
700
750
800
850

Supplementary Materials for

Low Coseismic Friction on the Tohoku-oki Fault Determined from
Temperature Measurements

Fulton, P. M., E. E. Brodsky, Y. Kano, J. Mori, F. Chester, T. Ishikawa, R. N. Harris, W.
Lin, N. Eguchi, S. Toczko and the Exp. 343/343T and KR13-08 Scientists

correspondence to: pfulton@ucsc.edu

This PDF file includes:

Materials and Methods
Supplementary Text
Figs. S1 to S9
Tables S1 to S2

Materials and Methods

Temperature Data

Temperature data were collected with 55 miniature temperature loggers (MTLs): 10 TDR-2050s and 15 TR-1050s manufactured by RBR Ltd. (Canada; **www.rbr-global.com/**) and 30 Antares 1357 high-pressure data loggers manufactured by Antares Datensysteme GmbH (Germany; **www.antares-geo.de/**). Each of the MTLs has an autonomous data logger and a temperature sensor enclosed within a titanium casing pressure rated for up to 10,000 m water depth. The TDR-2050s also have a pressure sensor that effectively records the sensor's water depth inside the cased borehole. The MTLs were attached to spectra rope and wrapped with a rubber protective covering. The sensor string was attached to a hanger and hung within 3.5" steel tube casing with a check-valve at the bottom that prohibited fluids from flowing into the casing from below. Spacing between sensors varied from 1.5 m at the bottom near the fault zone to 3 m, 6 m and greater intervals higher up. The sensors recorded every 10s, 20s or 10 minutes depending upon the model. The RBR temperature sensors have precision of <0.00005°C and the Antares 0.001°C. In addition to factory calibration constants, each temperature sensor was calibrated using a Hart Scientific water bath containing a mixture of ethylene glycol and water and an NIST reference temperature probe over 8 or more different temperatures from $0 - 30^{o}$C and spanning the range recorded during the JFAST experiment. The resulting sensor corrections permit accuracy for all temperature sensors to within ~0.001^{o}C. Reliable corrections could not be obtained for sensors at 744.77 and 805.17 mbsf. The absolute temperatures for these two sensors may be off by a few 10^{-3} ^{o}C , although their residual temperatures appear consistent with neighboring data. Additional details regarding the sensors and observatory are described in (*13*).

Thermal Properties

Knowledge of thermal-physical rock properties is important for interpreting the temperature data. Differences in thermal conductivity may lead to steady-state perturbations in the background geothermal gradient. Estimates of the thermal diffusivity are important for interpreting an observed temperature anomaly from frictional heating, and volumetric heat capacity controls the relationship between heat and temperature. We utilize thermal property measurements taken on core material from borehole C0019E that cover lithologic and depth intervals that correspond to the regions covered by sensors in the observatory. Thermal conductivity values consist of 45 shipboard measurements on split cores using a TEKA thermal conductivity half-space probe (*13*). An additional 38 discrete samples were also measured using a divided bar system revealing similar results. Four large samples were also measured using the transient plane heat source method revealing very little anisotropy in thermal conductivity. Thermal diffusivity and heat capacity measurements were also determined for these samples. The lowermost three samples are most representative of the intervals covered by sensors and the fault zone with the frictional heat signal and reveal average diffusivity and volumetric heat capacity values of 3.92 ± 0.5 x 10^{-7} m^2s^{-1} and 2.804 ± 0.32 MJ ^{o}C^{-1}m^{-3}. Large systematic changes in thermal conductivity are not observed over the intervals covered by temperature sensors (Fig. S2). There is, however, some difference in volumetric heat capacity and thermal diffusivity between the lowermost sample within subducting pelagic clays most

2

representative of the décollement fault zone and overlying mudrocks. This variability accounts for the largest source of uncertainty in our dissipated energy estimates.

Background geotherm / vertical heat flow

The average background geothermal gradient in the area of the frictional heat anomaly is calculated using a least-squares fit to data from 650 – 750 mbsf (n=18). This depth interval covers the hanging wall of the décollement where there is both abundant temperature and thermal conductivity data and above the frictional heat anomaly and areas of suspected heat advection by fluid flow. The data used for the fit are the daily average temperatures from an arbitrary day, 6 Dec 2012, that is well after drilling and installation so as to minimize any residual effects of drilling disturbance and before the nearby 7 Dec 2012 M_w7.4 earthquake which resulted in temperature perturbations. This value is relatively consistent throughout this time period, although there is a gradual steepening of the gradient due to reequilibration of the hole after drilling (Fig. S3). Error ranges reported in the main text for the gradient are 1 standard deviation determined by bootstrapping with 1000 realizations.

Thermal conductivity and temperature measurements are from separate boreholes, and thus we calculate the vertical heat flow by multiplying the least-squares fit thermal gradient by the average thermal conductivity values corresponding to the same depth and lithologic interval. To remove the background gradient for analysis of residual temperature (i.e. temperature minus a constant average background geotherm) we also utilize a least squares fit to the 5 data representative of positions above 650 mbsf (Fig. S1). Together the composite average background geotherm starts from a projected temperature at the sea floor of 2.50°C and increases by 27.57°C/km until 650 mbsf and then continues by 26.29°C/km to the bottom of the sensor string. The projected seafloor temperature of 2.50°C is larger than the observations taken at the seafloor of 1.7°C suggesting that thermal conductivity decreases at depths shallower than those covered by the observatory sensors.

Thermal conductivity as source of anomaly

If the thermal conductivity around the bottom part of the sensor string is much lower than the rest of the measurement depth range, it can result in a higher thermal gradient and hence a positive temperature anomaly as observed. Likewise, an increase in thermal conductivity can lead to a lower thermal gradient. The thermal conductivity λ necessary for a ΔT anomaly over a depth interval Δz is

$$\lambda = q_0 \bigg/ \left(\frac{q_0}{\lambda_0} + \frac{\Delta T}{\Delta z} \right) \qquad (S1),$$

where q_o and λ_o are the background vertical heat flow (30.50 ± 2.52 mW/m^2) and thermal conductivity (1.16 ± 0.09 W/m/K above the décollement fault zone), respectively.

Based on the JFAST observations, a 0.311 °C anomaly spread over ~20 m would require a thermal conductivity of 0.73 W/m/°C in the fault zone if the anomaly resulted from thermal conductivity variations alone.

Core samples within and around the décollement fault zone have a bulk thermal conductivity of 1.14 ± 0.07 W/m/$^{\circ}$C and porosities of $35.9 - 52.5\%$ implying matrix values of $\lambda_m \sim 1.39 - 2.13$ W/m/$^{\circ}$C. Bulk thermal conductivity λ_b for intimately mixed phases is appropriately modeled by:

$$\sqrt{\lambda_B} = \phi\sqrt{\lambda_w} + (1-\phi)\sqrt{\lambda_m} \qquad (S2),$$

where ϕ is porosity, λ_m is matrix conductivity, and λ_f is thermal conductivity of water which equals 0.6 W/m/$^{\circ}$C (*21*). Considering similar composition and λ_m value, a bulk thermal conductivity of 0.73 W/m/$^{\circ}$C requires porosities of $80 - 88\%$. Such large porosities are not apparent in logging or core observations from adjacent holes, suggesting thermal conductivity variation is an unlikely source for the observed positive heat anomaly along the plate boundary.

A localized increase in porosity by just 10% over a 20 m wide zone could result in reduction in thermal conductivity to values $\sim 1.01 - 1.04$ W/m/$^{\circ}$C and an apparent positive temperature anomaly by $0.05 - 0.07$ $^{\circ}$C. Direct measurements of thermal conductivity, including four measurements on highly sheared sections of the fault zone core itself, show no indication of such a large-scale systematic change in thermal conductivity within or around the fault zone (Fig. S2).

Drilling Anomaly

The perturbation due to drilling is modeled with a two-part synthetic. During drilling, seawater is circulated in the hole, and it is appropriately modeled as an isothermal line-source for the duration of drilling following reference (*8*). Heat is diffused axisymmetrically around the borehole. The resultant temperature disturbance as a function of time is

$$\Delta T_1(z,t) = [T_f - T_0(z)]\frac{Ei(-r_b^2 / 4\alpha(t - t_2)) - Ei(r_b^2 / 4\alpha(t - t_1(z)))}{Ei(-r_b^2 / 4\alpha(t_2 - t_1(z)))} \qquad (S3),$$

where T_f is the fluid temperature, $T_0(z)$ the rock temperature at the time of drilling, Ei is the exponential integral, r_c is the borehole radius, α is the thermal diffusivity of the formation, $t_1(z)$ is the time since the bit first penetrated to depth z, t_2 is the time drilling ends and fluid is no longer circulated.

During the casing installation, a cold pipe is lowered into the hole providing an instantaneous line sink of heat. On the center axis, the temperature disturbance is

$$\Delta T_2(z,t) = [T_c - T_0(z)](1 - e^{r_c^2 / 4\alpha(t - t_c(z))}) \qquad (S4),$$

where T_c is the casing temperature, r_c is the casing radius, and as before, $t_c(z)$ is the time of installation of the casing at depth z (*22*, p. 260).

Diffusion Model

The frictional temperature anomaly is modeled by the diffusion of heat from an infinitesimally thin planar source into the surrounding media. Although the thickness of a finite shear zone (*2a*) is important for constraining the maximum peak temperature within the fault during the earthquake, it is not a significant parameter for calculating the residual temperature anomaly at times longer than the characteristic diffusion time across the shear layer ($a^2/4\alpha$). The maximum possible thickness of the shear layer within the décollement plate boundary fault is 4.86 m (*6*) and commonly faults localize slip on zones on the order of 0.1-1 cm thick (*23*). The data studied here begin more than 1 year after the earthquake, so the appropriate model for the current data set is an infinitesimally thin plane:

$$\Delta T_{EQ}(z,t) = \frac{S}{2\sqrt{\pi\alpha(t - t_{EQ})}} e^{-(z-z_f)^2/4\alpha(t-t_{EQ})} \qquad (S5),$$

where t_{EQ} is the time of the earthquake, z_f is the depth of the fault, and the heat source, *S*, is the energy per m^2 dissipated by friction, i.e., $S=\tau d$ where τ is the shear stress on the fault during the earthquake and *d* is the slip distance. The recorded temperature as a function of depth and time is modeled as

$$T(z,t) - \left(\frac{dT}{dz}\right)_{gt} z = \Delta T_1 + \Delta T_2 + \Delta T_{EQ} \qquad (S6).$$

The most direct constraint from the data is on the dissipated energy *S*. Since the displacement is constrained from repeat seafloor bathymetry, the shear resistance τ is also readily interpretable. However, friction on faults is usually parameterized in terms of apparent coefficients of friction. Therefore, we take the extra step of relating the shear stresses to the equivalent apparent coefficient of friction by estimating the effective normal stress at the fault depth assuming hydrostatic pore pressure. The dip of the fault plane is low (5°) and for a near-horizontal fault zone the effective normal stress is equivalent to the effective lithostatic stress. For hydrostatic pore pressure, this is defined as,

$$\sigma_n' = \sigma_v' = (\rho_r - \rho_w)gz \qquad (S7).$$

Inversion Procedure

We inverted for the best-fit dissipated energy and depth by performing a gridsearch through apparent friction and depth and finding the combination of values that maximized the cross-correlation between the data from 800-820 mbsf and the model from Aug. 1 through Dec. 6, 2012 (Figs. 3 and S4-S5). For a given friction and depth combination, dissipated energy is uniquely determined and therefore the results can also be viewed as an optimization of dissipated energy and depth. Confidence intervals in Table S2 were computed by varying the thermal diffusivity and heat capacity with a normal distribution over their observed ranges (Table S1) and repeating the inversion for each realization of these thermal parameters (Fig. S6). The depth constrained inversion

5

assumed that the fault lies near the observed peak in the temperature between the deepest and the 3rd from the bottom sensor (Fig. 3).

We also calculated confidence intervals based on constant thermal parameters and bootstrapping the observed data. This procedure resulted in much smaller ranges of the inverted parameters. Therefore, the estimates based on a distribution of thermal parameters are preferred as a more accurate representation of the larger source of error.

<u>Radiated Energy</u>

Radiated energy estimates (*11, 12*) range from 3-9 x 10^{17} J, and assuming 5.4 x 10^{10} m^2 for the rupture area, result in an areal average of 8-17 MJ/m^2.

<u>Peak Temperature During Slip</u>

Although the observed temperature anomaly more than a year after the Tohoku earthquake is insensitive to the slip zone thickness and slip duration, by assuming these two parameters, estimates of the maximum peak temperature during slip can be made.

The temperature evolution of a frictional heat anomaly *T* for all times during and after slip can be described by (*25* adapted from *22, 26*),

$$\Delta T(x,t) = \frac{A_\circ}{\rho c} \left(\begin{array}{l} t\left[1 - 2i^2 erfc\left(\frac{a-x}{\sqrt{4\alpha t}}\right) - 2i^2 erfc\left(\frac{a+x}{\sqrt{4\alpha t}}\right)\right] \\ -H\left(t-t^*\right)\left(t-t^*\right)\left[1 - 2i^2 erfc\left(\frac{a-x}{\sqrt{4\alpha\left(t-t^*\right)}}\right) - 2i^2 erfc\left(\frac{a+x}{\sqrt{4\alpha\left(t-t^*\right)}}\right)\right] \end{array} \right)$$

(S8a),

for distances $x \le a$, where *a* is the half-width of the shear zone, and

$$\Delta T(x,t) = \frac{A_\circ}{\rho c} \left(\begin{array}{l} t\left[2i^2 erfc\left(\frac{x-a}{\sqrt{4\alpha t}}\right) - 2i^2 erfc\left(\frac{x+a}{\sqrt{4\alpha t}}\right)\right] \\ -H\left(t-t^*\right)\left(t-t^*\right)\left[2i^2 erfc\left(\frac{x-a}{\sqrt{4\alpha\left(t-t^*\right)}}\right) - 2i^2 erfc\left(\frac{x+a}{\sqrt{4\alpha\left(t-t^*\right)}}\right)\right] \end{array} \right)$$

(S8b),

for $x > a$, where *t** is the duration of heating (i.e. slip duration), α is the thermal diffusivity, ρ and *c* are the bulk density and heat capacity, respectively. The $i^2erfc(\xi)$ terms represent the second integral of the complementary error function evaluated from ξ to ∞ (*22*), and $H(\xi)$ is the Heaviside function, which is evaluated for $\xi = t - t^*$ such that the multiplied terms to the right are only applied when $t \ge t^*$. A_o is the volumetric frictional heat generation rate within the slip zone defined as

$$A_o = \frac{\tau d}{2at^*} \qquad \text{(S9)},$$

where d is the total slip distance on a particular slip zone. At times considerably greater than the characteristic diffusion time across the slip zone ($t \gg a^2/4\alpha$), the results of Eq. S8 and Eq. S5 become indistinguishable.

The maximum peak temperature above the background value occurs at $t = t^*$ and $x = 0$. Using the estimate for the average shear stress during slip τ determined above from the observed temperature anomaly, the maximum peak temperature increase is

$$\Delta T_{peak} = \frac{\tau d}{2a\rho c}\left(1 - 4i^2 erfc\left(\frac{a}{\sqrt{4\alpha t^*}}\right)\right) \qquad \text{(S10)}.$$

This equation assumes a constant slip velocity and shear stress during slip, which is a practical approximation that provides a reasonable estimate of peak temperature rise for comparison with geologic and geochemical indicators of frictional heating. Figure S7 shows results for a range of plausible slip durations and slip zone thicknesses.

Geochemical constraints on hydrogeology

Geochemical analysis of pore waters collected from Hole C0019E core samples provides insight into the hydrogeology of the JFAST site subsurface (Fig. S8). The Cl⁻ concentrations of pore waters are similar to seawater (SW), and a steady decrease from 800 mbsf to the bottom of the hole is observed. Such a decrease of Cl⁻ is generally explained by contribution of deep-seated fluid, which has been diluted with fresh water derived from the breakdown of hydrous minerals, such as illitization of subducted clay minerals. However, only a slight decrease of Cl⁻ is observed here (3% dilution) indicating limited contribution of deep-seated fluid compared to, for example, the décollement at the western Nankai trough (20% dilution; *27*). A striking feature of the depth profiles in C0019E is that most of major and minor components analyzed show steady-state increase/decrease below 800 mbsf. Such steady-state characteristics can be explained by vertical diffusive flow combined with in-situ diagenetic solid-fluid reaction (*27*). These observations combined with a lack of minimum or maximum around 820 mbsf suggests no significant active fluid flow along the plate boundary fault.

Other constraints on hydrogeology

Annular pressure while drilling borehole C0019B showed no indication of large overpressures or substantial fluid flow through any faults or fractures, including the décollement (*13*). The pressure data also show no evidence of large fluid losses into highly permeable faults or formations.

Zones of increased permeability, however, are more likely susceptible to a near-borehole infiltration of cold drilling fluids and thus a longer recovery of temperature from drilling disturbance and transient cold anomalies in early times. A depth profile of the characteristic recovery time of temperatures following drilling and observatory installation reveal two zones with anomalously long recovery times around 757 – 769

mbsf and 795 – 811 mbsf (Fig. S9). Both of these zones also record disturbances following a nearby M_w7.4 20 km deep normal faulting earthquake on 7 Dec 2012. Borehole circulation resulting from strong ground motions perturbs borehole temperature in the deeper parts of the borehole before quickly re-equilibrating with the formation. In addition, a gradual increase in temperature over ~1-2 weeks after the local earthquake is seen around 763 – 775 and 803 – 814 mbsf which may be indicative of transient fluid flow from depth up permeable conduits (Fig. 2, S9).

Variability in temperature as indicator of advection

     High-frequency variability in the daily-average temperature is clearly apparent at both 784 mbsf and 763 mbsf during periods when advective fluid flow in inferred within these zones (i.e. before and after the local 7 December 2012 earthquake, respectively) (Fig. S10). This temperature variability is correlative with neighboring sensors as well, suggestive of fluctuations in the degree advective fluid flow over time. We quantify the variability in temperature fluid flow by using a band-pass filter from 2.1 to 3.5 days and taking the standard deviation (Fig. S9D). We analyze the data at all depths for time periods from 1 August to 5 December, 2012 to represent times before the local M_w7.4 7 December, 2012 earthquake. After the earthquake we analyze times from 10 December, 2012 (after a few days of borehole reequilibration following strong motion mixing within the borehole) to 24 April, 2013. The locations of large variability are consistent with other indications of high permeability. The data within the décollement fault zone ~820 mbsf do not reveal large variability, providing additional evidence to suggest the anomaly at this depth is not a result of advective fluid flow.

Supplementary Text

Additional Author notes:

     The list of group author "Expedition 343 /343T and Kairei Cruise KR13-08 scientists": Masanori Kyo (CDEX-JAMSTEC, Japan), Yasuhiro Namba (CDEX-JAMSTEC, Japan), Hiroaki Muraki (Marine Works Japan, Japan), Takafumi Kasaya (JAMSTEC, Japan), Marianne Conin (CEREGE, France), J. Casey Moore (University of California Santa Cruz), Yasuyuki Nakamura (JAMSTEC, Japan), Louise Anderson (University of Leicester, UK), Becky Cook (University of Southampton, UK), Tamara Jeppson (University of Wisconsin-Madison, USA), Monica Wolfson-Schwehr (University of New Hampshire, USA), Yoshinori Sanada (JAMSTEC, Japan), Saneatsu Saito (JAMSTEC, Japan), Yukari Kido (JAMSTEC, Japan), Takehiro Hirose (JAMSTEC, Japan), Jan Behrmann (IFM-GEOMAR, Germany), Matt Ikari (University of Bremen, Germany), Kohtaro Ujiie (University of Tsukuba, Japan), Christie Rowe (McGill University, Canada), James Kirkpatrick (Colorado State University, USA), Santanu Bose (University of Calcutta, India), Christine Regalla (The Pennsylvania State University, USA), Francesca Remitti (Universitá Modena e Reggio Emilia, Italy), Virginia Toy (University of Otago, New Zealand), Toshiaki Mishima (Osaka City University, Japan), Tao Yang (Institute of Geophysics, China Earthquake Administration, China), Tianhaozhe Sun (University of Victoria, Canada), James Sample (Northern Arizona University, USA), Ken Takai (JAMSTEC, Japan), Jun Kameda (The University of Tokyo, Japan), Lena Maeda (JAMSTEC, Japan), Shuichi Kodaira (JAMSTEC, Japan), Ryota Hino (Tohoku University, Japan), Demian Saffer (The Pennsylvania State
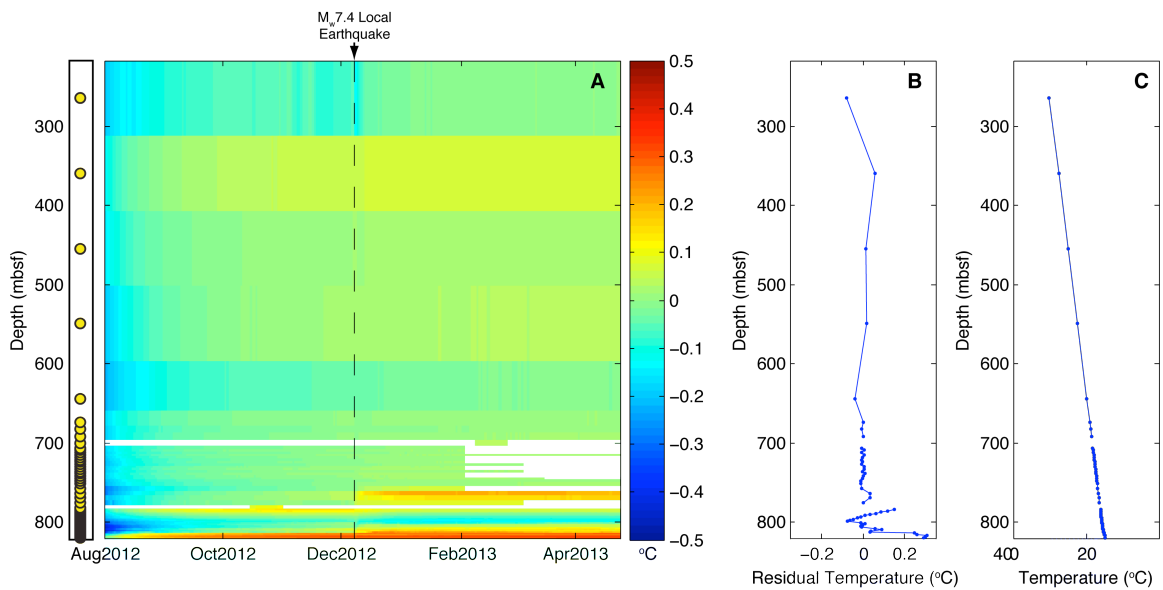
University, USA).

Fig. S1.

Subseafloor residual temperature field. Similar to Fig. 2. (A) Time/space map of all data between 1 August 2012 and 24 April 2013. A close up view of data >650 mbsf is shown in Fig. 2. Yellow dots show sensor positions and each row represents each sensor's data. Each column is the daily average temperature after an average background geotherm is removed. A local M_w7.4 earthquake occurred 17:18:30 JST on 7 Dec 2012 (dashed line). The second deepest sensor (818.51 mbsf) failed on Sept. 22, 2012; subsequent data in that row is interpolated from sensors 1.5 m above and below. Periods of no data collection are otherwise shown by white. (B) Depth profile from 1 Dec. 2012. (C) Depth profile from 1 Dec. 2012 of temperature without background geotherm removed.
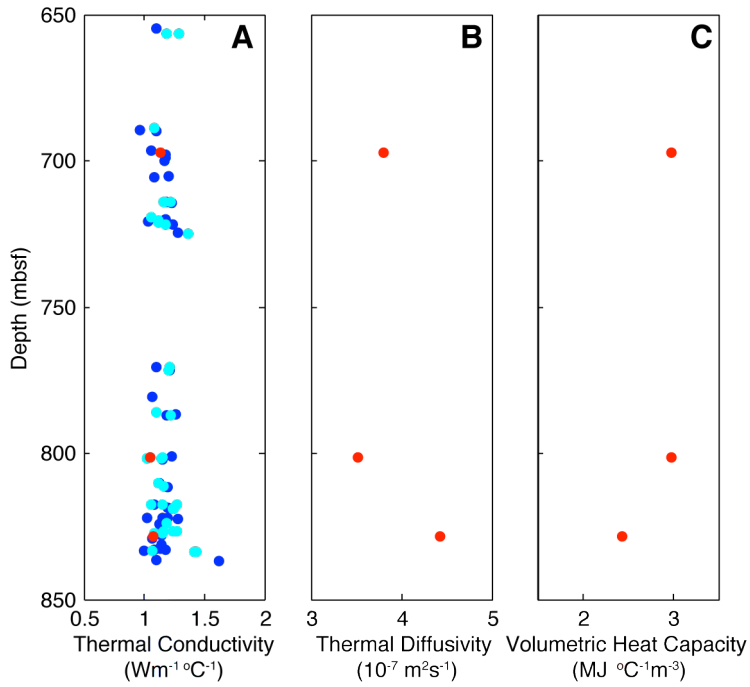
Fig. S2

Thermal Properties. (A) Thermal conductivity, (B) thermal diffusivity, and (C) volumetric heat capacity. All measurements were performed on core samples from hole C0019E. Colors represent data source: blue (*13*); cyan (divided bar measurements); red (transient plane heat source measurements).
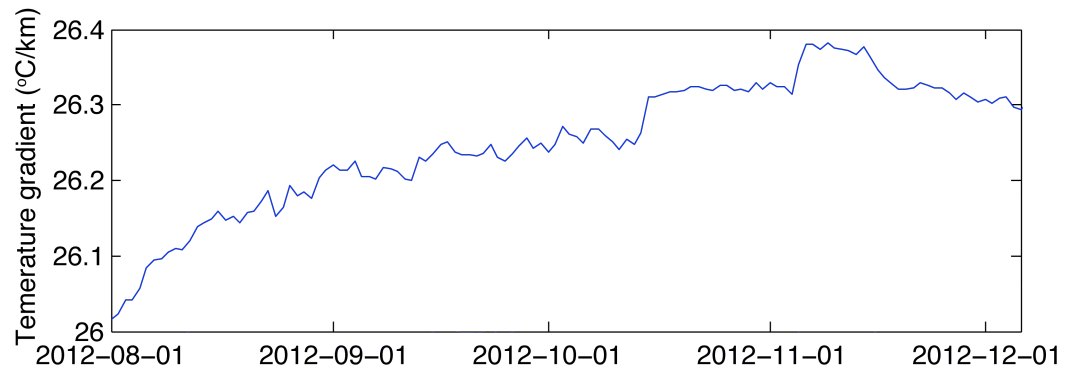
Fig. S3

Temperature gradient over time. Least-squares fit temperature gradient for data between 650 and 750 mbsf for times between 1 August 2012 – 6 Dec 2013.
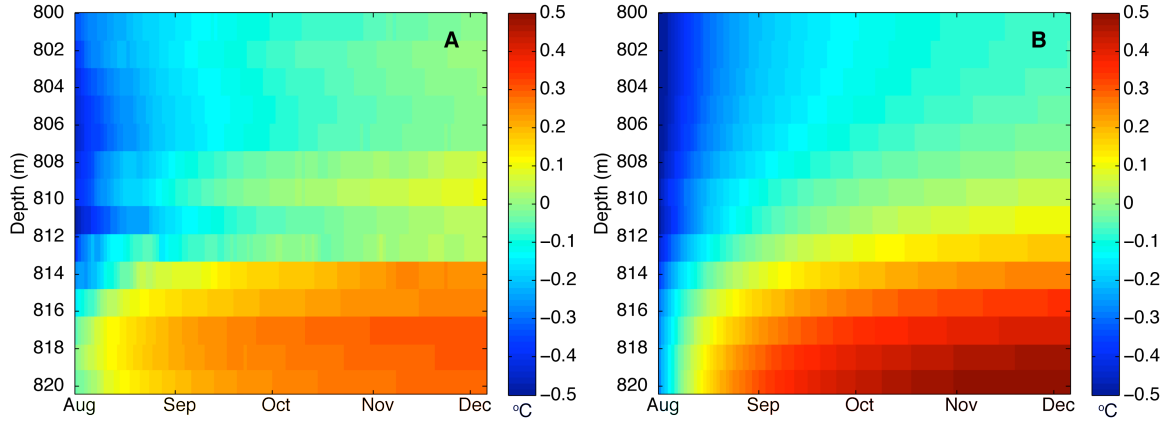
Fig. S4

Time/space map of residual temperature near inferred slip zones. (A) The same as Fig. 3A, a close-up view of the residual temperature anomaly near the plate boundary from 1 August - 6 December 2012. (B) Simulated residual temperature from model inversions in which fault depth is unconstrained.
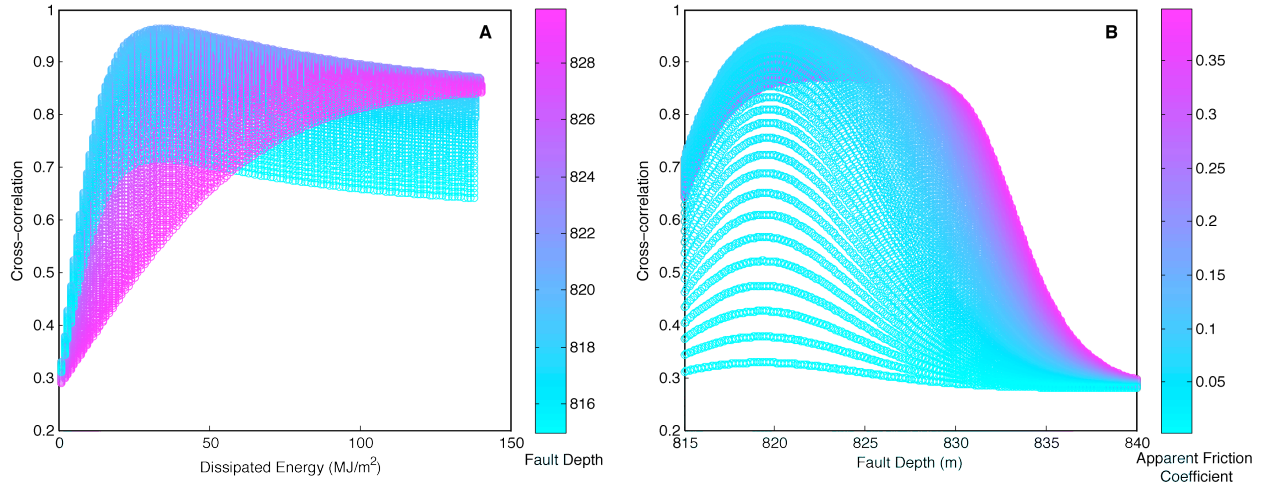
Fig. S5

Cross-correlation of residual temperature from model and observed data for a wide range
of depths. Free parameters were apparent coefficient of friction and the depth of the fault.
Panel A shows the cross-correlation for different dissipated energy values with color
indicating different fault depth locations. Panel B shows the cross-correlation as a
function of fault depth with color indicating the apparent friction coefficient derived from
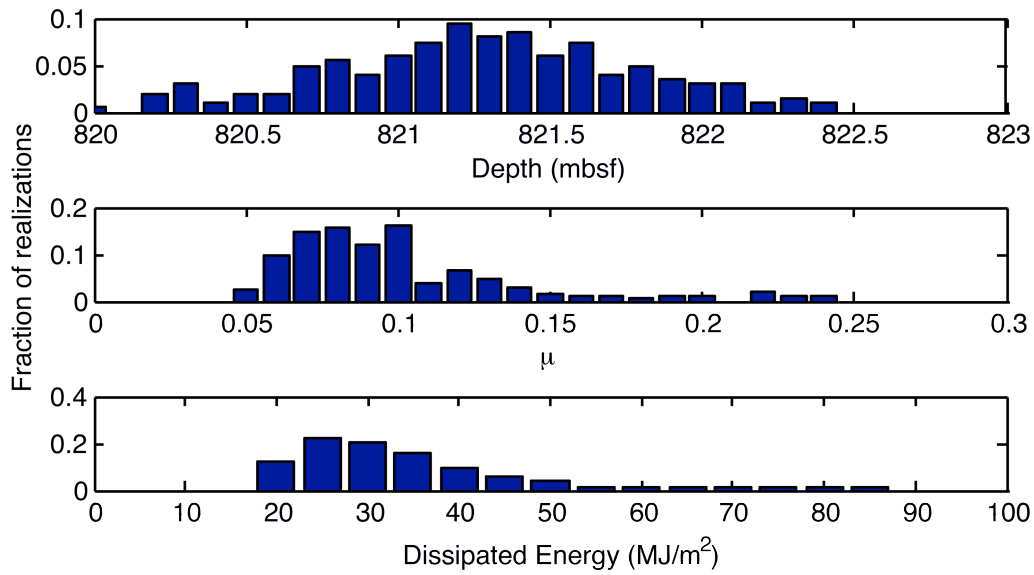different values of dissipated energy.

Fig. S6

Normalized distribution of optimal fault depth, apparent friction μ, and dissipated energy from 200 model inversion realizations with unconstrained depth. The variability in the inversion results stems from allowing the thermal diffusivity and heat capacity to randomly vary over their measured ranges (See text).
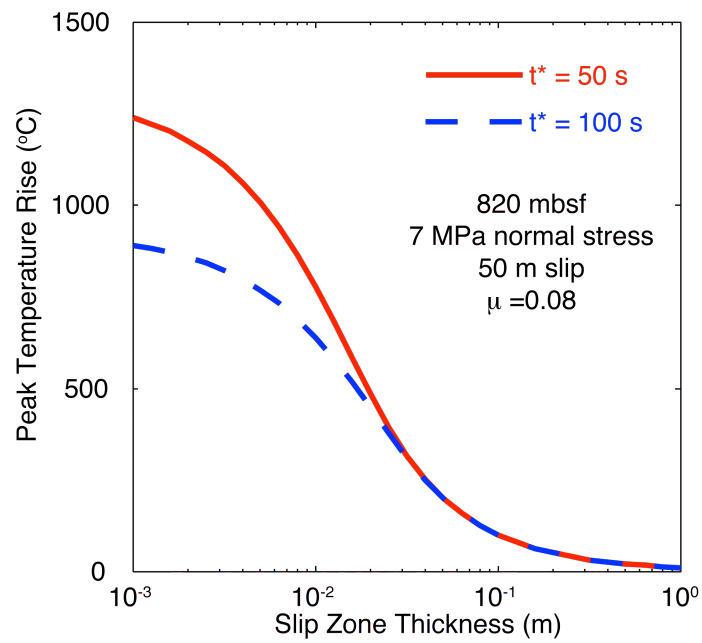
Fig. S7

Peak temperature estimate. Estimate of peak temperature within the fault slip zone for different assumed slip zone thicknesses and slip durations.
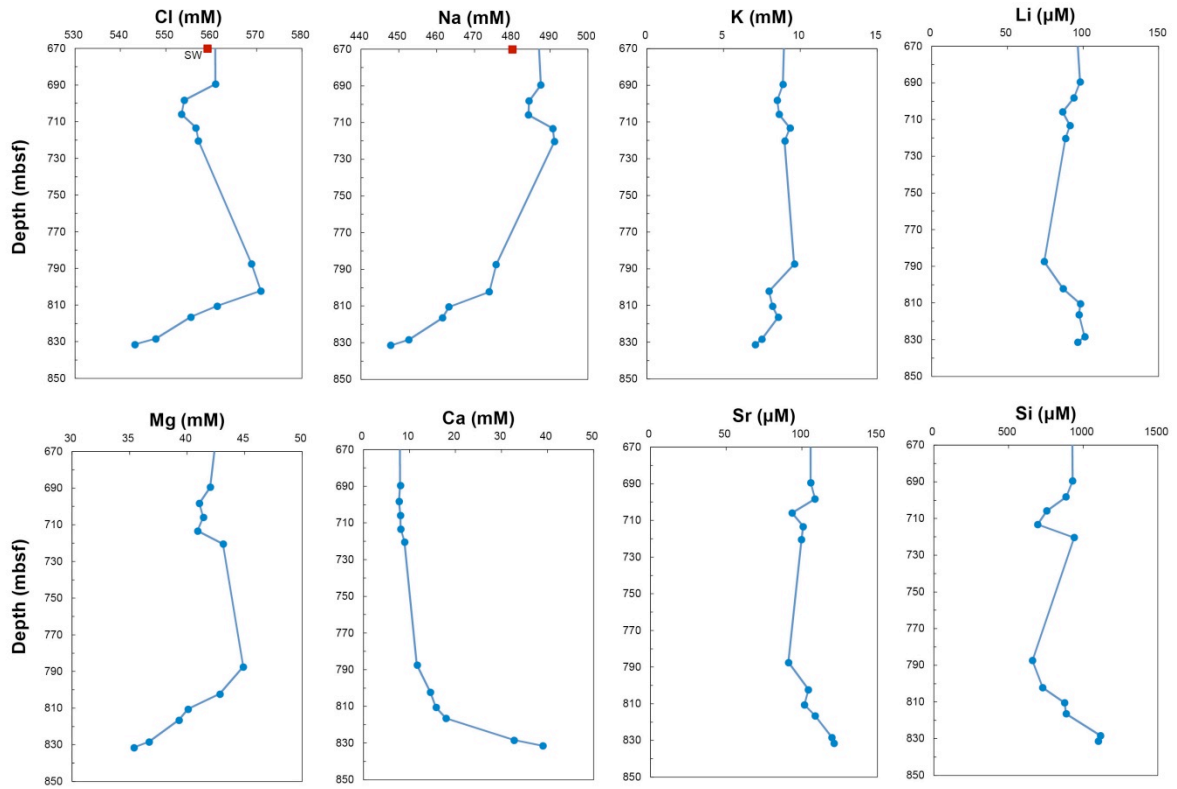
Fig. S8

Pore water geochemistry. Depth profiles of representative pore water geochemistry data from Hole C0019E (*13*).
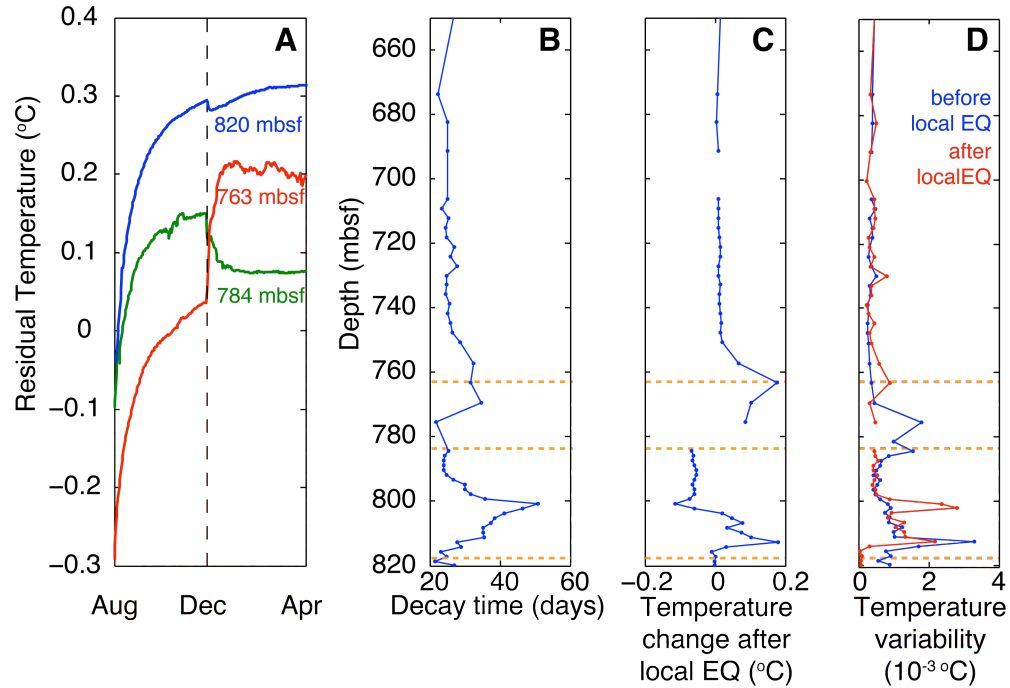
Fig. S9

Permeability Indicators. (A) Time evolution of residual temperature at the plate boundary at around 820 mbsf (blue), 784 mbsf (green), and 763 mbsf (red). Time of $M_w7.4$ local earthquake on 7 Dec 2012 is shown by dashed line. (B) Depth profile of the characteristic decay time at each sensor depth. Anomalously high decay times may indicate areas of permeable fractures / damage zones in which cold drilling fluids were able to infiltrate during drilling. Locations of 820, 784, and 763 mbsf are shown by orange dashed lines. (C) Change in residual temperature in response to the $M_w7.4$ local earthquake on 7 Dec 2012 calculated as difference in mean daily temperature at each depth between 6 Jan 2013 and 6 Dec 2013. (D) The standard deviation in temperature variability, as described in the supplemental text, for times before the local 7 Dec 2012 earthquake (blue) and times after the earthquake (red).

Table S1.

Modeling Parameters.

Parameter	Value	
Drilling fluid temperature T_f	1.7°C	Measured seafloor temperature
Casing temperature T_c	1.7°C	Measured seafloor temperature
Thermal diffusivity α	$3.92 \pm 0.05 \times 10^{-7}$ m^{2}s^{-1}	Average of 3 representative samples
Thermal conductivity K	1.14 ± 0.07 W/m/°C	Average of 38 representative samples
Volumetric heat capacity ρc	2.804 ± 0.32 MJ °C^{-1}m^{-3}	Average of 3 representative samples
Casing radius r_c	0.1079 m	
Borehole radius r_b	0.1079 m	
Geothermal Gradient $(dT/dz)_{gt}$	26.293°C/km	Measured
Dip of Fault θ	5°	
Slip distance d	50 m	*(8)*
Static coefficient of friction μ_s	0.2	*(27)*
Density of rock	1850 kg/m^3	Measured on discrete samples >650mbsf (*7*)
Density of water	1000 kg/m^3	

Table S2.

Inversion results and confidence intervals.

Depth Constrained inversion	**Median Value**	**90% Confidence Interval**
Depth	819.8 mbsf (7717.3 mbsl)	819.8 mbsf (7717.3 mbsl)
Apparent coefficient of friction	0.08	0.05-0.15
Dissipated energy	27 MJ/m^2	19-51
Slip-averaged shear stress	0.54 MPa	0.38-1.0 MPa
Unconstrained inversion		
Depth	821.3 mbsf (7718.8 mbsl)	820.3-822.1 mbsf (7717.8 -7719.6 mbsl)
Apparent coefficient of friction	0.09	0.06-0.20
Dissipated energy	31 MJ/m^2	20-69 MJ/m^2
Slip-averaged shear stress	0.63 MPa	0.40-1.4 MPa